Materials Today Physics 34 (2023) 101091

Contents lists available at ScienceDirect

Materials Today Physics

journal homepage: www.journals.elsevier.com/materials-today-physics

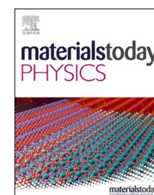

Metallization and superconductivity with *Tc* > 12 K in transition metal dichalcogenide HfS_2 under pressure

S. Rahman [a,f,***], Linyan Wang [b], H. Saqib [c], D. Errandonea [d], Li Yang [a], Yongsheng Zhao [c], Yukai Zhuang [e], Guoying Gao [b,**], Lin Wang [b,c,*], Yongjun Tian [b]

[a] School of Physics and Optoelectronic Engineering, Hangzhou Institute for Advanced Study, University of Chinese Academy of Sciences, Hangzhou, 310024, China
[b] Center for High Pressure Science (CHiPS), State Key Laboratory of Metastable Materials Science and Technology, Yanshan University, Qinhuangdao, Hebei, 066004, China
[c] Center for High Pressure Science and Technology Advanced Research, Shanghai, 201203, China
[d] Departamento de Física Aplicada-ICMUV, MALTA Consolider Team, Universidad de Valencia, Edificio de Investigación, C/Dr. Moliner 50, Burjassot, 46100, Valencia, Spain
[e] Institute of Atomic and Molecular Physics, Sichuan University, Chengdu, 610065, China
[f] University of Chinese Academy of Sciences, UCAS, China

A R T I C L E I N F O

Keywords:
Phase transition
Pressure effects
Superconducting phase transition
Electronic & structural properties
Density of states

A B S T R A C T

The application of high pressure not only drives the comprehension of the structure and triggers exotic electronic states in transition metal dichalcogenides, but also promotes the discovery of intriguing phenomena. Here, we show that HfS_2 exhibits highly tunable electronic property under pressure with sequence of gradual narrowing of band-gap at <40 GPa, followed by pressure-induced metallization at above 40 GPa, and ultimately superconductivity starting at ~115 GPa. Raman and x-ray diffraction experiments provide strong evidence for first-order structural phase transitions from a trigonal ($P\overline{3}m1$) to an orthorhombic (*Immm*) at around 18 GPa and then to a tetragonal structure (*I*4/*mmm*) above 40 GPa. The disappearance of all the Raman modes supported the observed metallization at above 40 GPa. At the similar pressure, the carrier-type of the sample is found to transform from electron to hole according to the Hall coefficient. At a critical pressure of 115 GPa a superconducting state sets with a transition temperature (*Tc*) of 3 K. Further compression dramatically increases *Tc* up to a maximum value of 12.2 K at 173 GPa, setting a record of *Tc* for superconducting transition metal dichalcogenides with zero-resistance. The pressure-induced high *Tc* superconductivity is closely linked to structural reconstructions which trigger changes in electronic states near the Fermi surface. The efficient and remarkable manipulation on the transport properties of 1T-HfS_2 not only shed lights on the broad perspective of layered materials but also provide crucial information towards their practical applications.

1. Introduction

As a new family of two-dimensional (2D) materials, transition metal dichalcogenides (TMDs) [1] have gained a great deal of attention due to their rich physical properties and intriguing applications [2,3], especially in electronics and optoelectronics. There are two fundamental polytypes of layered TMDs with the chemical formula MX_2 (M = Ti, Nb, Ta, Mo, Hf, W; X = S, Se, Te), known as (2H) and (1T). They are composed of layers of metal atoms coordinated in a trigonal prismatic (2H) or an octahedral (1T) manner [4,5]. Some of these materials exhibit superconductivity when tuning the electronic and crystalline structure by various techniques [6]. The advent of superconductivity in these materials has attracted much attention and there has been significant development in recent years because of their promising physical

* Corresponding author. Center for High Pressure Science (CHiPS), State Key Laboratory of Metastable Materials Science and Technology, Yanshan University, Qinhuangdao, Hebei, 066004, China.
** Corresponding author. Center for High Pressure Science (CHiPS), State Key Laboratory of Metastable Materials Science and Technology, Yanshan University, Qinhuangdao, Hebei, 066004, China.
*** Corresponding author. School of Physics and Optoelectronic Engineering, Hangzhou Institute for Advanced Study, University of Chinese Academy of Sciences, Hangzhou, 310024, China.
E-mail addresses: Saqibrahman@ucas.ac.cn (S. Rahman), gaoguoying@ysu.edu.cn (G. Gao), linwang@ysu.edu.cn (L. Wang).

https://doi.org/10.1016/j.mtphys.2023.101091
Received 31 December 2022; Received in revised form 11 April 2023; Accepted 18 April 2023
Available online 20 April 2023
2542-5293/© 2023 Elsevier Ltd. All rights reserved.

properties, such as continuous phase transitions, high transition temperature (*Tc*), and enhanced parallel critical magnetic field [7]. Researchers are also beginning to focus on these 2D materials because the decreased dimension not only provides a fine-tuning electronic platform for the discovery of novel physical phenomena in the 2D confinement, but also facilitates the acquisition of deeper theoretical insights.

Generally, the electronic structure of TMDs has been tuned by controlling the spin splitting using electric fields [8–11], adjusting the sample thickness, using quantum confinement [9,12,13], or combining pressure and temperature [4,14,15]. Another method for tuning the electrical structure of TMD's is to apply stress or strain [13,16]. However, pressure and temperature are the most effective and clean ways of tuning the electronic states as well as lattice parameters since they do not introduce chemical disorder [14,15]. In various TMDs materials, numerous pressure-induced structural, magnetic, and electronic transformations are observed, but little is known about the influence of pressure on 1T-HfS_2 [14]. 1T-(HfS_2) is a narrow band-gap semiconductor [17], that has a well-matched optical band gap with the solar spectrum and high electron affinity making it a promising element of a high-performance tunnel field-effect transistors (TFET) [18], infrared optoelectronic devices, and photovoltaic cells [19]. However, a theoretical and experimental analysis of the structural and physical properties of HfS_2 under high pressure has never been carried out. Multiple recent studies imply that tuning the band structure or carrier densities will be critical for many of its prospective applications, including optoelectronics devices. These aspects inspire us to tune the electrical and structural properties of HfS_2 under extreme compression.

In this article we study the structural and electronic properties of pristine 1T-HfS_2 under compression by combining various experimental techniques including resistivity, Raman scattering, and synchrotron X-ray diffraction (XRD) along with density-functional theory (DFT) calculations. We observed a structural phase transition from a trigonal (P $\overline{3}$ m1) to an orthorhombic (*Immm*) structure followed by another transition to a tetragonal structure (*I4/mmm*) after 40 GPa, accompanied by a carrier-type inversion and a successive semiconductor-metal transition. We also found, according to electrical transport measurements, that HfS_2 exhibits superconductivity with $Tc = 3$ K at 115 GPa. Under further compression, *Tc* increased from 3 K at 115 GPa to 12.2 K at 173 GPa. We discovered that the emergence of the superconductivity can be attributed to the change of the electronic structure, possibly related to the enhancement of the density of states (DOS) at high pressure. Finally, a pressure-temperature phase diagram establishes a correlation of structural transitions and electrical transitions with distinct electronic states.

2. Results

2.1. Pressure-induced superconductivity

Layered HfS_2 is a semiconductor with indirect and direct optical band-gaps of 1.28 and 2.07 eV, respectively [20–22]. Fig. 1 depicts the resistivity under compression at room temperature (RT) (a) and during cooling at different pressures (b-d). Upon compression, the resistivity of HfS_2 significantly drops from ambient pressure to approximately 15 GPa. From this pressure to 60 GPa the resistivity keeps decreasing but with a smaller slope. The large decrease of resistivity can be explained assuming an intrinsic semiconductor. In fact, a decrease in band-gap energy, as determined by calculations, will account for the observed drop in resistivity up to 15 GPa. The resistivity above 60 GPa is

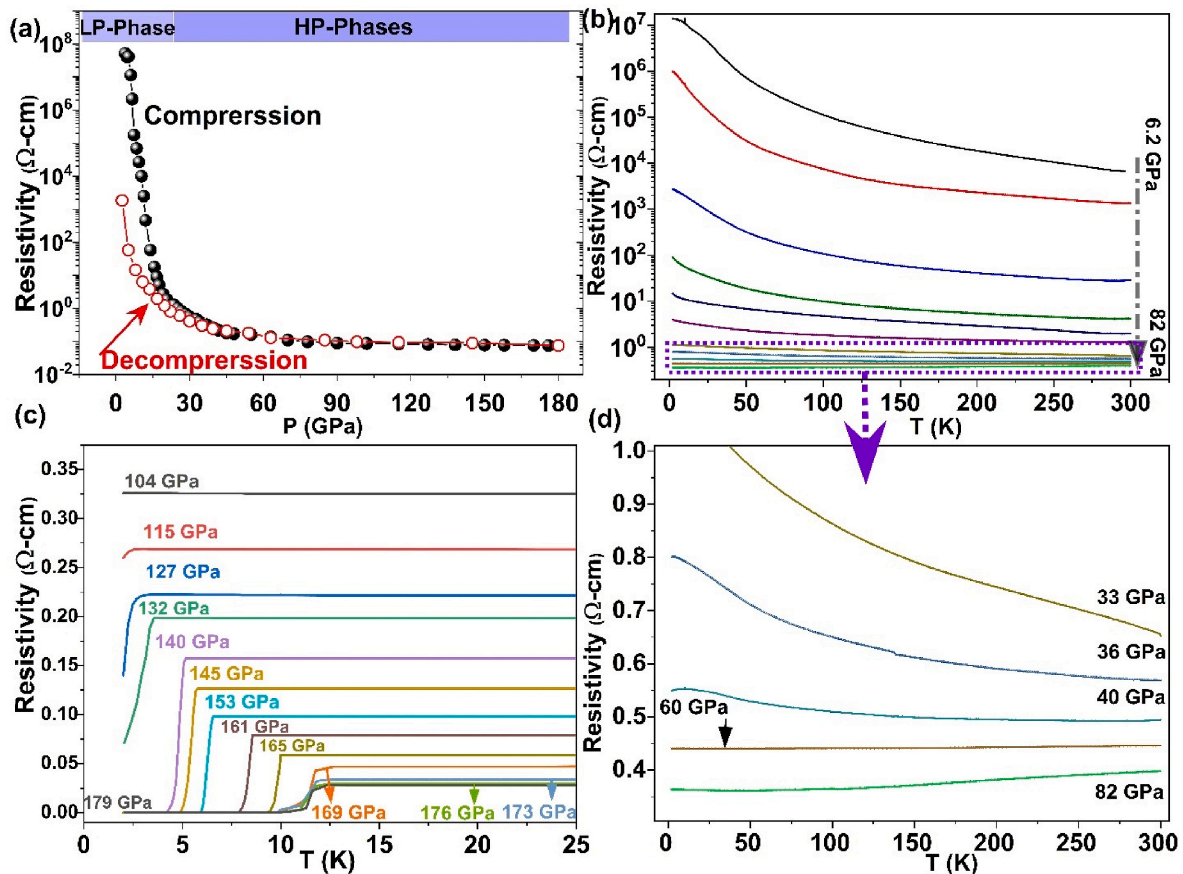

Fig. 1. (Color online); (a) Resistivity of HfS_2 as a function of pressure at RT. (b) Temperature dependence of the resistivity at different pressures (6.2–82 GPa). (c) Temperature-resistivity curves at different pressures (104–179 GPa) restricted to $T < 25$ K. (d) Temperature dependence of the resistivity of few pressures illustrate the semiconductors-metal transition.

comparable to the high end of resistivity values for metals at room temperature indicating a transition from semiconductor to metal [23, 24]. Metallic behavior at 60 GPa can be seen clearly in Fig. 1(d) These findings agree with the outcomes of our band-structure calculations. Pressure-induced electrical resistivity changes in HfS_2 can be separated into three sections. In the low-pressure range (LP, 1–18 GPa), resistivity falls from $\rho = 1.6 \times 10^8$ Ω cm to $\rho = 2.1 \times 10^2$ Ω cm with slope d $ln(\rho)$/dP = 0.66 ± 0.006 GPa^{-1}. This precipitous drop is due to a narrowing of the band gap. The change in the behavior at 18 GPa is due to the emergence of a new phase coexisting with the low-pressure phase (as shown below). In the region of phase coexistence, the resistivity decreases to ρ = 12 Ω cm as the low-pressure and high-pressure (*Immm*) phase coexists. Then, the resistivity reaches values around ρ = 0.4 Ω cm which is smaller than the typical resistivity of semiconductors. Finally, the decrease of ρ eventually saturates at the level approximately 0.3 Ω cm indicating that HfS_2 evolves toward a HP metallic phase (*I4/mmm*). This pressure-induced semiconductor-to-metal transition is verified by the temperature-dependent resistance measurements presented in the following section.

To confirm the pressure-induced metallization and get more thorough understanding of electrical properties, temperature-dependent resistivity measurements were performed from 6.2 GPa to 179 GPa at temperatures as low as 2 K. As illustrated in Fig. 1(b–d), and S2(Sup. Mat.); three regimes can be identified upon compression. Initially, at pressures below 20 GPa, a typical semiconductor behavior is observed as negative dρ/dT is recorded at all temperatures. There is no other resistance anomaly found in the entire temperature range of the low-pressure phase. Secondly, above 40 GPa positive dρ/dT is recorded for all temperatures, supporting a metallic behavior of HfS_2. Thirdly, from 100 GPa onward the resistivity exhibits a metallic state (dρ/dT > 0) between 300 K and 13 K without superconductivity behavior below this temperature. Interestingly, at 115 GPa we observed a dramatic drop in resistance at 3 K. Upon further compression, the resistance drop grows sharply and becomes increasingly obvious, and eventually zero-resistivity state is reached at 140 GPa which suggests a pressure-induced superconductivity (SC) with a superconducting *Tc* of 4.1 K at 140 GPa.

To further characterize and confirm the superconductivity, we measured the temperature-dependent resistivity of the sample at various magnetic fields at 142 GPa [Fig. 2(a)]. It is found that the drop of resistance shifts to lower temperature with increasing magnetic field and the superconducting state is about to vanish at the applied magnetic field~1.8 T [25]. These findings reveal that the pressure-induced resistance drop is a consequence of a superconducting transition. From our measurements we extracted the field dependence of midpoint *Tc* for HfS_2 at 142 GPa. We determine the upper critical magnetic field at zero temperature ($\mu_0 Hc_2(0)$) to be about ~2.2 T [Fig. 2(b)] by fitting the $\mu_0 Hc_2(T)$ with the conventional one-band Werthamer-Helfand Hohenberg (WHH) theory [26–28] and 3.1 T when the Ginzburg-Landau (GL) theory [25,29,30] is used. Details of empirical Formulas are given in supplemental Note 10. We note that the derived value of $\mu_0 H_{c2}(0)$ is much lower than the Pauli limiting field for a singlet pairing of $\mu_0 H_P(0) = 1.84 T_c$ [31], which is 8.8 T for *Tc* = 4.8 K.

Another intriguing characteristic we revealed is the evolution and variation of the *Tc* with the application of pressure, shown in Fig. 1(c) and 2(c). The superconducting transition with a zero-resistance state increases from 3 K to 12.2 K with increasing pressure then gradually levels off at 176 GPa.

We have summarized the *Tc* of various superconducting TMDs in Table S1 (supplemental material), which included the ionic liquid gating and high-pressure modulation. As can be seen, the highest *Tc* value obtained in this study is clearly higher than all the previously reported superconductivity temperatures with a zero-resistance state for TMDs. The superconducting critical temperature of 12.2 K in compressed HfS_2 hence sets a record of *Tc* in all superconducting TMDs.

To investigate the underlying changes in the electronic band structure of the sample, we studied the Hall effect at various pressures using the van der Pauw method by applying different external magnetic fields (0–6 T) at 10 K. Results of the Hall-effect coefficient (R_H) are provided in Fig. 3. We found that R_H is negative at 7 GPa, implying that HfS_2 is a n-type semiconductor. In the pressure range of a coexistence of LP (P $\overline{3}$ m1) and HP (*Immm*) phases (18–25 GPa), R_H remains negative. The magnitude of R_H decreases with pressure implying an increase of free-carrier concentration, which is consistent with the decrease of both the resistivity and the band-gap energy [32–34]. The R_H value varies from negative to positive above ~40 GPa. The observed change in the sign of R_H is the consequence of a carrier-type inversion induced by pressure [34–36] and it might be associated with structural changes. The positive sign of the Hall coefficient after the phase transition implies that hole-carriers are dominant at the high-pressure phase (*I4/mmm*). After this carrier-type inversion, R_H decreases, i.e. the carrier concentration increases. The values of R_H above 100 GPa corresponds to carrier concentrations of the order of 10^{21} cm^{-3}, which is consistent with the observed metallization. It suggests that the structural phase transition enhances the contribution of hole carriers which seems to be in favor of superconductivity at higher pressure beyond 120 GPa.

2.2. Structural transition under pressure

To understand the observed transport behavior of pristine 1T-HfS_2, we examined the crystal structure transformations by DFT calculations and experimental observations. Firstly, we carried out structural prediction calculations to find out the ground state structure at ambient conditions and subsequently at higher pressures. The CALYPSO structure search method has been successfully applied to predict structures in

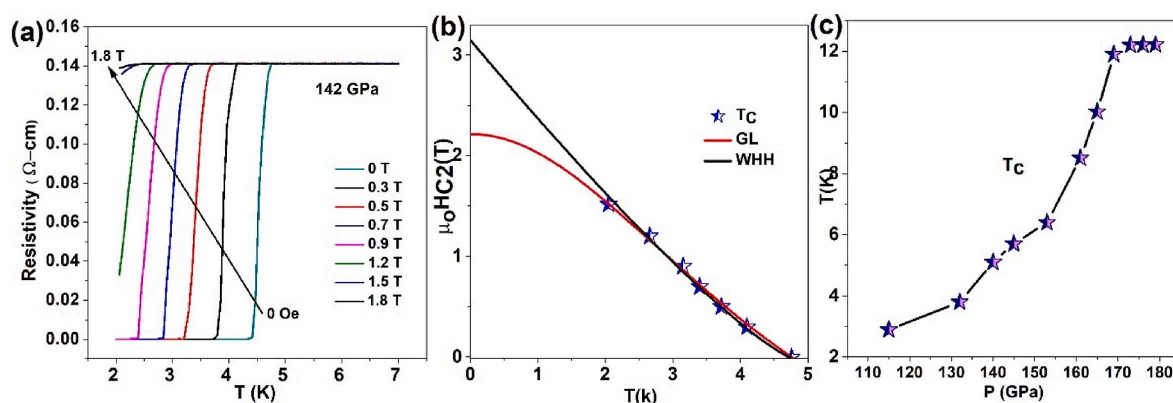

Fig. 2. (Color online) (a) Temperature dependence of resistivity under different magnetic fields at 142 GPa. (b) $\mu_0 H_{c2}$-T phase diagram. The solid line represents fitting by the GL & WHH theory. (c) Variation of *Tc* with increase pressure.

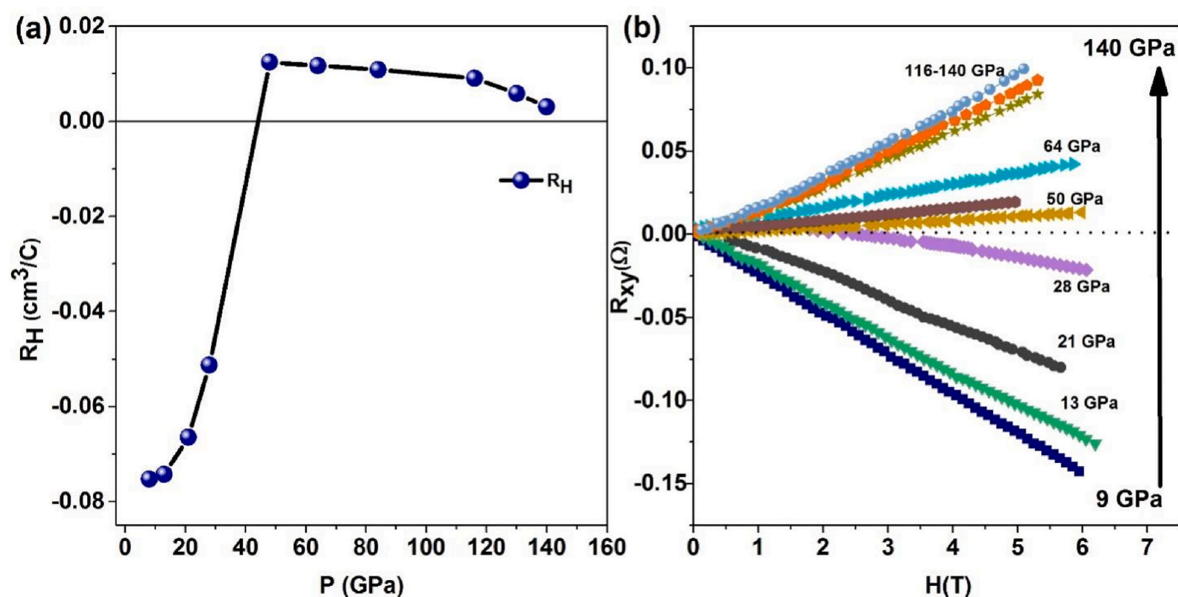

Fig. 3. (a) Pressure dependent Hall coefficient (R_H) at 10 K (b) Hall resistance as a function of applied magnetic field at 10 K under different pressures.

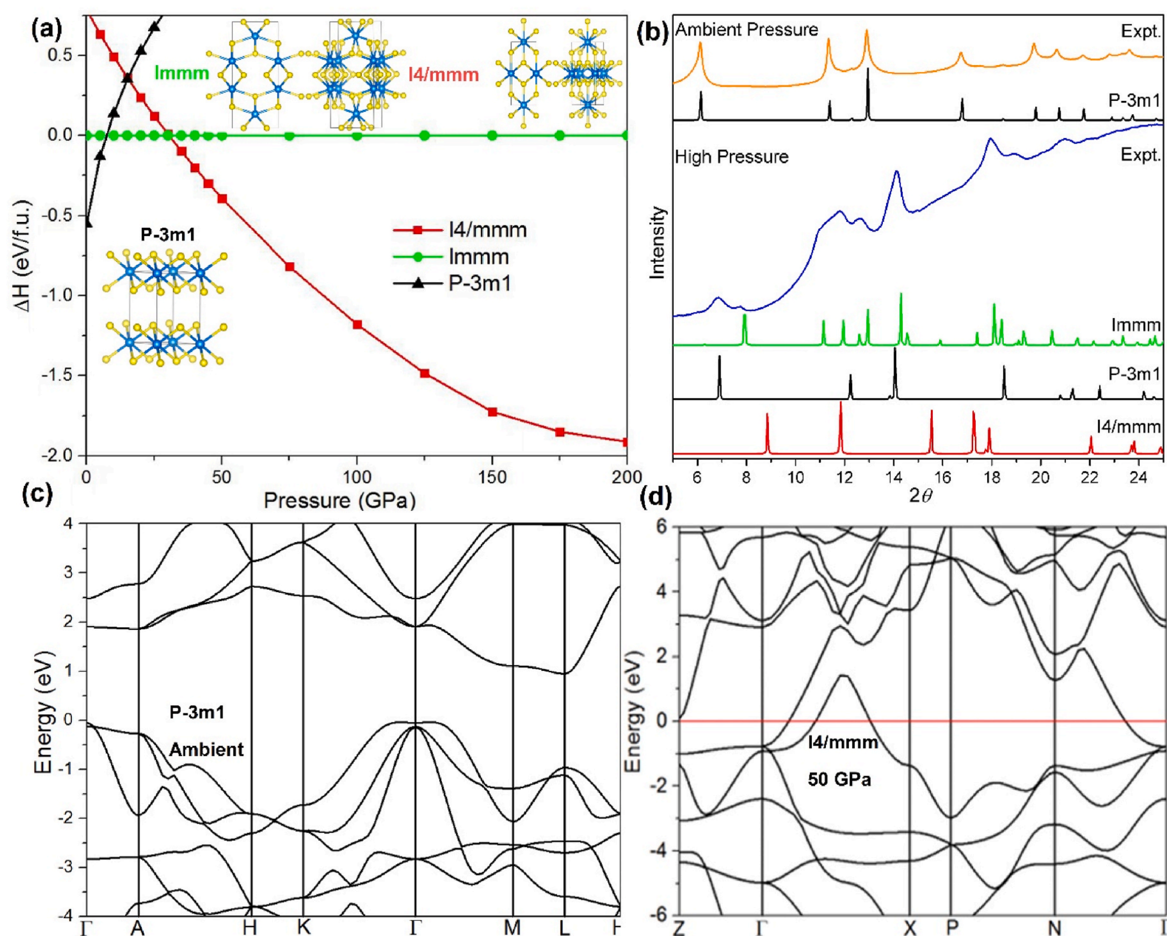

Fig. 4. (Color online) (a): The relative enthalpy of the predicted structures with respect to *Immm*under pressure. (b) Comparison of the calculated and experimental crystal structure of P-3m1 at ambient, and HP predicted and experimental crystal structures (*Immm* & *I4/mmm*) around 25 GPa (λ = 0.6199) (c–d) Calculated band structure of HfS_2 at ambient and 50 GPa.

the pressure range from ambient to 200 GPa. Details of calculation are given in supplemental Note 1. Structural relaxations were based on DFT within the Perdew-Burke-Ernzerhof (PBE) parametrization of the generalized gradient approximation (GGA) [37] as implemented in the Vienna ab initio simulation package [38]. The enthalpies of various structures under pressure are shown in Figure 4(a). At ambient conditions, HfS_2 compound adopts a trigonal crystal phase (space group P $\overline{3}$ m1) and matched well with the known structure (see ICSD Collection Code: 638847). Moreover the calculated phase at ambient is in good agreement with the experimental result as shown in Fig. 4(b). The enthalpy difference curves for predicted structures shows a phase transition from P $\overline{3}$ m1 to *Immm* (orthorhombic) and then a transformation to a tetragonal structure (*I4/mmm*). The simulated XRD pattern of high-pressure phase (*Immm*) at 25 GPa is depicted in Fig. 4(b). The calculated transition pressure is in good agreement with the experimental result. Changes in enthalpy illustrate that beyond 40 GPa the *I4/mmm* structure is energetically more favorable and a more stable structure under pressure than P $\overline{3}$ m1 and *Immm* phases. Upon further increase of pressure, (*I4/mmm*) remains the most stable phase up to the highest pressure of 200 GPa. Simulated XRD patterns of HfS_2 with the *I4/mmm* HP structure at 150 GPa can be seen in Fig. S5(c). The low-pressure trigonal phase supports a semiconducting behaviour and the high-pressure phase transition supports the huge drops of resistivity indicating the emergence of metallic behaviour.

To confirm the predicted structures, we examined the crystal structure by high-pressure XRD measurements as shown in Fig. S5(a). It is found that all peaks can be indexed well with the trigonal phase in the P $\overline{3}$ m1 space group at ambient pressure. We found that XRD patterns up to 18 GPa can be refined with the same structure; indicating that ambient pressure phase of HfS_2 is stable below 18 GPa as shown in Figs. S5(a) and S4(a) (supplementary material). However, an additional peak appears at $\sim 12.5^\circ$ with a shoulder peak at 14° when pressure is increased to 21.3 GPa, and its intensity increases with pressure, indicating that the pressure induces a phase transformation. This fact and the changes in the shape and intensity of the several peaks indicate the onset of a phase transition.

The new phase coexists with the ambient-pressure phase in a pressure range of 18–25 GPa, as depicted in Fig. S5. At 25 GPa, the XRD pattern of the high pressure phase became dominant and were successfully refined by the orthorhombic space group (*Immm*). With additional compression up to 30 GPa, the absence of any significant changes in the XRD pattern confirms the stability of the high-pressure phase (*Immm*). These experimental observations are in good agreement with the formentioned theoretical calculations.

Based on our XRD results, we extract the pressure dependence of lattice parameters and unit-cell volume before and after the phase transition as illustrated in Fig. S6. Fig. S6(a) shows the behavior of the lattice parameters with compression in the low-pressure phase ($P\overline{3}m1$). In this phase the unit-cell parameter c is 4.3% more compressible than a. This can be explained by the fact that the in-plane covalent bond is much stronger than the van der Waals bonding between neighboring planes. Increases in pressure cause sulfur atoms to move closer together, the repulsive force between sulfur atoms in neighboring layers develops dramatically and becomes comparable to the Hf–S intra-bond, causing the compressibility of the c axis to decrease slowly. So, the large axial anisotropic compressibility is associated with weak van der Waals interlayer forces and the strong intralayer covalent bonding. Aksoy et al. found discontinuities in the reduction of cell parameters and volume due to the *c*-axis being relatively more compressive between a specific pressure range, which has been interpreted as evidence of a phase transition [39]. In our case, for more structural information, the unit-cell volume as a function of pressure was fitted with the third-order Birch-Murnaghan equation of state [40,41]. The fitting results yield the low-pressure phase (P $\overline{3}$ m1) volume $V_0 = 66.9$ Å^3, with a bulk modulus of $B_0 = 55$ GPa and for the high-pressure phase (*Immm*) volume $V_0 = 60$ Å^3, with a bulk modulus of $B_0 = 59$ GPa. Decompression indicates that the transition is partially reversible and have signature of HP phase (see Fig. S5(a).

Raman spectra of HfS_2 as a function of pressure at RT are shown in Fig. S5(b). According to group theory 1T-HfS_2 has six optical modes $\Gamma = A_{1g} + E_g + A_{2u} + E_u$. The modes $A_{1g} + E_g$ are Raman-active [22,42,43]. The frequency of the Raman modes is given in Table S2. All modes are found to harden with increasing pressure. Around 14 GPa, two extra peaks appear with one shoulder peak next to the $A1_g$ mode as shown in Fig. S5(b). This is due to the onset of the phase transition, which has been observed in our HP XRD measurements. The shoulder peak becomes dominant at 20.7 GPa and can be certainly attributed to a high-pressure phase (orthorhombic-*Immm*) of HfS_2. In addition to the two extra peaks, discontinuity in the pressure shift, and variations in the rate of shift vs pressure of the original modes support the transition discovered by XRD and electrical transport studies. Detailed information about the Raman modes is illustrated in the Supplemental Material (Note 4). Further compression leads to the disappearance (reduced intensity and merged with background) of all Raman modes after 40 GPa. The disappearance of Raman signals associated to structural transformation and domination of *I4/mmm* (tetragonal structure) as well as conductivity changes and occurrence of metallization [44]. Like the electrical transport data and XRD, the Raman spectrum did not fully return to its original feature upon decompression to ambient pressure manifesting the partially reversible structural transition as illustrated in Fig. S3. The mode-Grüneisen parameters (γ) were obtained for both LP (P $\overline{3}$ m1), and HP (*Immm*) phases with the equation: $\gamma = K_0/\omega_0(d\omega/dP)$ by using the bulk modulus (K_0) determined from XRD. They range from 0.47 to 0.65 and 0.21–0.38 for the LP and HP phase, respectively as illustrated in Table S3.

2.3. Interpretation by theoretical calculations

To better understand the topological property of HfS_2, the physics of the observed superconductivity as well as stability of high pressure phases, we performed the DFT calculations on the electronic band structures and surface states, as shown in Fig. 4(c–d) & S1(a). The electronic band structures and density of states (DOS) were investigated by using a HSE06 hybrid functional. The band structures along high symmetry Γ-M–K-Γ directions in Brillouin zone of HfS_2 at various pressures are shown in Fig. 4(c–d), S1(a). The results clearly show the narrowing of the band gap of the low-pressure phase (P $\overline{3}$ m1), which however, does not show the metallic character up to 19 GPa. The calculations also show that the HP phase (I4/mmm) is metallic after 40 GPa supporting our experimental observations.

The results clearly demonstrate the band gap narrowing of the low-pressure phase (P $\overline{3}$ m1), which is compatible with transport measurements. At ambient pressure, our band structure calculations demonstrate a semiconducting ground state of HfS_2 with a band gap of about 1.28 eV consistent with previous results and current experimentally observed value of 1.2 eV. Upon compression, a narrowing of the indirect band gap takes place. This phenomenon is caused by the movement of the bottom of the conduction band towards the Fermi level. Notice that the decrease of the band gap does not involve changes in the topology of the band structure, retaining HfS_2 an indirect semiconductor characteristic up to the transition pressure. It can also be observed in the figure that band gap of low-pressure phase (P $\overline{3}$ m1) is decreasing with increase pressure, but it is still in semiconducting state even at 20 GPa as the conduction band minimum is still above the Fermi level. Fig. 4(d)-S1(a) illustrates band structure of HP phase above 40 GPa, around which the band gap become narrow, signaling the semiconductor-to-metal transition associated with the structural transition. Notice that the metallic character of the HP phase (*I4/mmm*) is fully consistent with the weakening and ultimately disappearance of the Raman signal.

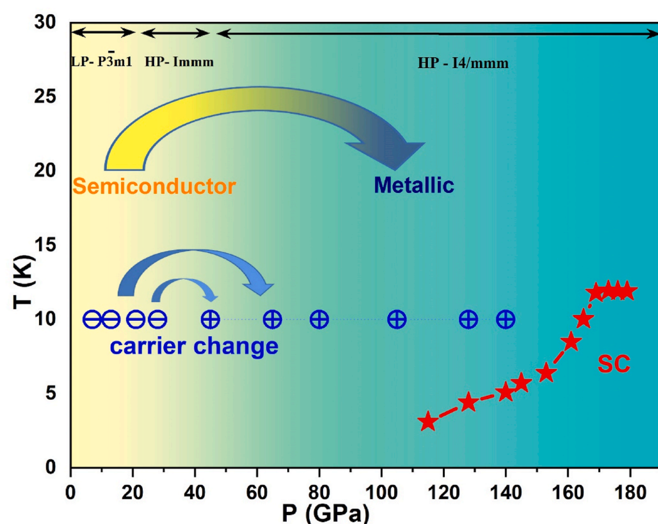

Fig. 5. (a)Pressure-temperature (P–T) phase diagram of IT- HfS_2. The vertical yellow and blue shades demarcate the semiconducting and metallic states, respectively, also illustrating the low-pressure and high-pressure structural phases. (−) sign shows type and ⊕ shows p type carrier and (*) shows superconducting *Tc*.

3. Discussion

Fig. 5 schematically summarizes our results. The vertical yellow and blue shades demarcate the semiconducting, metallic and superconducting states respectively which depicts the low pressure and high-pressure structural phases, revealing a significant correlation between electronic and structural changes in 1T- HfS_2 in range of 0–180 GPa.

Numerous changes in the Raman spectrum and XRD patterns show compelling evidence of structural transformations from trigonal (P $\bar{3}$ m1) to tetragonal (*I*4/*mmm*). For the structures starting with van der Waals interactions at ambient conditions, the modification of pressure sensitive van der Waals forces is usually accompanied by first-order structural transitions [45]. Usually tetragonal structures described by space group P4/mmm, $I4_1/amd$, and *I*4/*mmm*, have been found to be the most stable structures under high pressure above 100 GPa for various TMDs, such as 1T-TiS_2, 1T-$HfSe_2$, 2H–$NbSe_2$, 2H–MoS_2, 2H–NbS_2, 2H–$MoSe_2$, and 1T′-ReS_2 [46–50]. Above 18 GPa, our findings are consistent with a structural transition from trigonal (P $\bar{3}$ m1) to orthorhombic (*Immm*) and finally to tetragonal (*I*4/*mmm*) phases. We are unable to get experimental structure information above 30 GPa, but we can hypothesize from previous studies in TDMs and our calculations that the structure described by space group *I*4/*mmm* is stable at high pressure. In our previous work on 1T-$HfSe_2$, we observed that the pristine 1T structure eventually transforms to a *I*4/*mmm* phase with enhanced superconductivity under high pressure [41]. It is similar with the experimentally and theoretically calculated high pressure phases of $HfSe_2$ [41, 51], in which the second transition to space group *I*4/*mmm* was predicted after 40 GPa. Moreover, in our present study of HfS_2, the metallization process entails changes to both the electronic and crystal structures, whereas the superconducting transition is independent of the structural transformation. Pressure-induced interlayer distance reduction is thought to be a key factor in the HfS_2 metallization process. To understand the metallization of HfS_2, one must understand the role of pressure-induced interlayer distance reduction and effect of carrier concentration. The change in value of hall coffecient (R_H) above 40 GPa, indicates the transformtion from electron-type carriers to hole-type carriers, which is might be associated with structural and band-gap changes. Thus, we speculate that the pressure-induced structural modulation in HfS_2 results in the electronic states changes near the Fermi surface, which induces the emergence of SC. It suggests that the structural phase transition enhances the contribution of hole carriers which seems to be in favor of superconductivity at higher pressure beyond 120 GPa. We are confident that the experimental superconducting phase is likely *I*4/*mmm* because, firstly, it is the most stable metallic phase at high pressure and, secondly, it have been the most favorable and predominate phase for superconductivity at ultrahigh pressure. We also calculated the e-p coupling with a *Tc* of 0.7 K at 160 GPa, although this result is lower than the experimental value.

Figs. 2–5, S1 illustrates the complimentary evidence of the superconducting transition and metallization where the band structure of LP (P $\bar{3}$ m1) phase shows semiconducting behavior, and the HP (*I*4/*mmm*) phase shows metallic behavior. The modern approaches used in this article and the observed phase transitions involve versatile phase-control factors (such as temperature, pressure) creating new platforms and the resulting phases have also provided opportunities to explore novel 2D physics in the future.

In conclusion, we have explored the high-pressure evolution of the structural and transport properties for HfS_2, one of the van der Waals-type layered materials, by XRD, Raman, resistivity, and Hall coefficient measurements. 1T-HfS_2 undergoes a pressure-induced (P $\bar{3}$ m1 –*Immm* - *I*4/*mmm*) transformations above 18 GPa accompanied by a successive charrier-type inversion and a semiconductor-metal transition. The phase transition is confirmed by Raman spectroscopy and the metallization associated with it by *ab-initio* electronic band structure calculations. Upon further compression, superconductivity is triggered by pressure, the superconducting *Tc* increases progressively from ~3 K at 115 GP to ~12.2 K at 173 GPa, and then becomes almost stable. The extensive and continuous tuning of its electronic structure could be potentially used for energy-variable (IR-visible) optoelectronics and photovoltaics applications.

4. Experimental section

Sample Growth & High-pressure Experiments: HfS_2 crystals were purchased from HQ-graphene for our experiments. Diamond-anvil cells (DAC) with stainless steel gaskets were used with anvils with 300 μm culets for the XRD measurements and Raman. High-pressure synchrotron XRD measurements were conducted on the BL10XU beam line of Spring-8. Electrical transport measurements were carried out using a DAC made of non-magnetic Cu–Be alloy. An insulating gasket was prepared with a mixture of epoxy and cubic boron nitride for electrical measurements.

Theoretical Calculation Methods: Density-functional theory (DFT) calculations were performed to complete the experiments. Structure searches were performed using the particle swarm optimization technique as implemented in the CALYPSO code [52,53].

Detailed information about these experiments and calculation methods are illustrated in the Supplemental Material (Note.1).

Credit author statement

Saqib Rahman: Conceptualization, Methodology, Software, Writing – original draft preparation, Data curation, Investigation, Validation, Linyan Wang: Software. Data curation, Formal analysis, Hajra Saqib: Data curation, Visualization, Investigation. Validation, D. Errandonea: Writing- Reviewing and Editing, Resources, Formal analysis, Validation, Li Yang: Software, Validation, Formal analysis, Yongsheng Zhao: Validation, Data curation, Yukai Zhuang: Data curation, Formal analysis, Guoying Gao: Writing- Reviewing and Editing, Software. Data curation, Formal analysis, Resources, Lin Wang: Supervision, Writing- Reviewing and Editing, Funding acquisition, Project administration, Conceptualization, Yongjun Tian:Writing- Reviewing and Editing.

Declaration of competing interest

The authors declare that they have no known competing financial interests or personal relationships that could have appeared to influence the work reported in this paper.

Data availability

No data was used for the research described in the article.

Acknowledgements

This work was mainly supported by Natural Science Foundation of China (Grant Nos. 52090020, 52022089, and 52288102). D.E. thanks the support by the Spanish Ministerio de Ciencia e Innovación and Agencia Estatal de Investigación (MCIN/AEI/10.13039/501100011033) under grants PID2019-106383GB-C41 and RED2018-102612-T (MALTA Consolider-Team network) and by Generalitat Valenciana under grant Prometeo CIPROM/2021/075 (GREENMAT) and MFA/2022/007. S.R. thanks the support by Hangzhou Science and Technology Bureau of Zhejiang Province (TD2020002)

Appendix A. Supplementary data

Supplementary data to this article can be found online at https://doi.org/10.1016/j.mtphys.2023.101091.

References

[1] Y.I. Joe, et al., Nat. Phys. 10 (2014) 421.
[2] M.N. Ali, et al., Nature 514 (2014) 205.
[3] I. Pletikosić, et al., Phys. Rev. Lett. 113 (21) (2014): 216601.
[4] Z. Chi, et al., Phys. Rev. Lett. 120 (3) (2018): 037002.
[5] Z. Ye, et al., Nature 513 (2014) 214.
[6] C.S. Snow, et al., Phys. Rev. Lett. 91 (13) (2003): 136402.
[7] D. Qiu, et al., Adv. Mater. 33 (18) (2021): 2006124.
[8] H. Yuan, et al., Nat. Phys. 9 (9) (2013) 563.
[9] Y. Zhang, et al., Nat. Nanotechnol. 9 (2) (2014) 111.
[10] C. Wang, et al., Phys. Rev. Lett. 123 (12) (2019): 126402.
[11] H. Yuan, et al., Nat. Nanotechnol. 9 (10) (2014) 851.
[12] D.Y. Qiu, et al., Phys. Rev. Lett. 111 (21) (2013): 216805.
[13] W.S. Yun, et al., Phys. Rev. B 85 (3) (2012): 033305.
[14] Z. Zhao, et al., Nat. Commun. 6 (2015) 7312.
[15] Z.-H. Chi, et al., Phys. Rev. Lett. 113 (3) (2014): 036802.
[16] Y.Y. Hui, et al., ACS Nano 7 (8) (2013) 7126.
[17] M.J. Mleczko, et al., Sci. Adv. 3 (8) (2017): e1700481.
[18] S.H. Chae, et al., ACS Nano 10 (1) (2016) 1309.
[19] Q.H. Wang, et al., Nat. Nanotechnol. 7 (11) (2012) 699.
[20] S.N. Neal, et al., npj 2D Materi. Appl. 5 (1) (2021) 45.
[21] M. Traving, et al., Phys. Rev. B 63 (3) (2001): 035107.
[22] J. Ibáñez, et al., Sci. Rep. 8 (1) (2018): 12757.
[23] D.C. Giancoli, Physics, fourth ed., Prentice Hall, 1995.
[24] H. Nguyen, et al., J. Phys. Soc. Jpn. 81 (2012) SB041. Suppl.B.
[25] P. Müller, et al., The Physics of Superconductors: Introduction to Fundamentals and Applications, Springer Berlin Heidelberg, 2013.
[26] O. Pavlosiuk, et al., Sci. Rep. 5 (1) (2015) 9158.
[27] Q. Dong, et al., npj Quantum Mater. 6 (1) (2021) 20.
[28] Y. Qi, et al., Nat. Commun. 7 (1) (2016): 11038.
[29] L. Fang, et al., Phys. Rev. B 72 (1) (2005): 014534.
[30] J.A. Woollam, et al., Phys. Rev. Lett. 32 (13) (1974) 712.
[31] A.M. Clogston, Phys. Rev. Lett. 9 (6) (1962) 266.
[32] Y. Li, et al., AIP Adv. 8 (11) (2018): 115202.
[33] D. Errandonea, et al., Phys. Rev. B 55 (24) (1997): 16217.
[34] J. Zhang, et al., Appl. Phys. Lett. 103 (8) (2013): 082116.
[35] J. Guo, et al., Front. Electron. Mater. (2022) 2.
[36] D. Errandonea, et al., High Pres. Res. 26 (4) (2006) 513.
[37] J.P. Perdew, et al., Phys. Rev. Lett. 78 (7) (1997) 1396.
[38] G. Kresse, J. Furthmüller, Phys. Rev. B 54 (16) (1996): 11169.
[39] R. Aksoy, et al., J. Phys. Chem. Solid. 67 (9–10) (2006) 1914.
[40] E. Greenberg, et al., High Pres. Res. 29 (4) (2009) 764.
[41] S. Rahman, et al., Phys. Rev. B 105 (9) (2022): 094307.
[42] N. Glebko, et al., J. Phys. Chem. C 122 (47) (2018): 26835.
[43] M. Grzeszczyk, et al., Pressure-driven Phase Transitions in Bulk HfS2, 2021.
[44] S. Rahman, et al., Mater. Today Phys. 25 (2022): 100698.
[45] H. Yang, et al., Nat. Phys. 13 (10) (2017) 931.
[46] D. Zhou, et al., J. Alloys Compd. 757 (2018) 448.
[47] Z.-L. Liu, et al., J. Alloys Compd. 610 (2014) 472.
[48] D. Zhou, et al., npj Quantum Mater. 2 (1) (2017) 19.
[49] M. Li, et al., Semicond. Sci. Technol. 36 (9) (2021): 09LT02.
[50] O. Kohulák, et al., Phys. Rev. B 91 (14) (2015): 144113.
[51] C. Tian, et al., Phys. Rev. B 105 (18) (2022) L180506.
[52] Y. Wang, et al., Phys. Rev. B 82 (9) (2010): 094116.
[53] Y. Wang, et al., Comput. Phys. Commun. 183 (10) (2012) 2063.